PAPER

Metal–organic framework-derived nanoflower and nanoflake metal oxides as electrocatalysts for methanol oxidation†

W. Kamal,[a] Abeer Enaiet Allah,[a] Rehab Mahmoud,[a] Ahmed A. Farghali,[b] Amna A. Kotp[b] and Abdalla Abdelwahab [ID] *[ac]

The energy crisis is the most urgent issue facing contemporary society and needs to be given top priority. As energy consumption rises, environmental pollution is becoming a serious issue. Direct methanol fuel cells (DMFCs) have emerged as the most promising energy source for a variety of applications such as electric vehicles and portable devices. Unfortunately, the kinetics of methanol oxidation is slow and needs an electrocatalyst to improve the reaction kinetics and the overall fuel cell efficiency. Herein, a straightforward hydrothermal procedure was utilized to prepare copper, nickel, and cobalt-based MOF composites by altering the elemental molar ratios. Cu-MOF (MOFP1), Cu/Ni-MOF (MOFP2), and Cu/Ni/Co-MOF (MOFP3) were prepared after carbonization and characterized using several key techniques such as FTIR, XRD, SEM, and EDX. The SEM analysis reveals that the morphology of MOFP1 is spherical aggregated particles, while that of MOFP2 or MOFP3 is in the form of nanoflakes and nanoflowers. Moreover, upon application of these composites as electrocatalysts for methanol electro-oxidation in an alkaline medium of 1 M NaOH using cyclic voltammetry (CV) and chronoamperometry (CA) tests, the electrochemical performance of MOFP2 in 1 M methanol exhibits the best performance for methanol oxidation with a current density reaching 38.77 mA cm^{-2} at a scan rate of 60 mV s^{-1}. This can be attributed to the unique porous open flower structure and the synergistic effect between copper, nickel, and 2-aminoterephthalic acid which develop its catalytic activity.

[a]Department of Chemistry, Faculty of Science, Beni-Suef University, 62514 Beni-Suef, Egypt. E-mail: aabdelwahab@psas.bsu.edu.eg
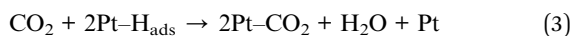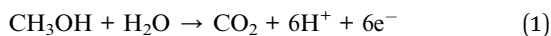
[b]Materials Science and Nanotechnology Department, Faculty of Postgraduate Studies for Advanced Science (PSAS), Beni-Suef University, 62511 Beni-Suef, Egypt

[c]Department of Chemistry, College of Sciences, University of Ha'il, Ha'il, 81451, Saudi Arabia. E-mail: a.abdelsalam@uoh.edu.sa

† Electronic supplementary information (ESI) available. See DOI: https://doi.org/10.1039/d4ra04902k

1. Introduction

Energy is a critical component of the link between nature and mankind, and it has an economic impact.[1] One of the most pressing issues confronting the globe today is how to generate energy in a sustainable and low-cost manner. Another goal is to reduce the environmental threat posed by global warming and to provide a solution to the scarcity of fossil resources.[2] Because of the growth of this technology, renewable energy systems are now considered as highly effective and ecologically beneficial power generation alternatives. Renewable energy systems are characterized by low environmental impact, simple design, high power conversion efficiency (up to 50–55%) regardless of scale, generation of useful heat for power generation, integration with gas turbines and fuel flexibility.[3]

Innovations in the field of fuel cells provide a safe way to generate electrical energy from chemical energy with high direct conversion efficiency and low environmental impact.[4] Direct methanol fuel cells (DMFCs) have emerged as the most promising energy source for a variety of applications such as electric vehicles and portable devices. The anodic reaction of DMFCs is the electrocatalytic oxidation of methanol.[5] Using methanol as a fuel has many advantages, including low working temperatures, easy storage and transportation, high energy efficiency, and rapid commissioning.[6] Methanol is an excellent fuel due to its high heating value (HHV), ease of production, and availability.[7,8] Unfortunately, the kinetics of methanol oxidation is very slow that needs an electrocatalyst to improve the reaction kinetics and the overall fuel cell efficiency.

Platinum acts as an extremely effective electrocatalyst for the oxygen reduction reaction (ORR) and fuel oxidation process (which includes hydrogen, methanol, ethanol, and formic acid).[9,10] Its superior performance is related to its distinctive electrical arrangement, which makes it easier to move electrons to and from methanol.[11] Despite these advantages, its high cost of utilization is the main obstacle to the commercialization of fuel cells.[1,12] In addition, its efficiency as an electrocatalyst is quickly diminished by the adsorbed carbon monoxide (CO) and

carbon dioxide (CO_2) species on the Pt surface, which causes poisoning and clogging surface during MOR.[1,13–16]

$$CH_3OH + H_2O \rightarrow CO_2 + 6H^+ + 6e^- \qquad (1)$$

$$2Pt + H_2 \rightarrow 2Pt-H_{ads} \qquad (2)$$

$$CO_2 + 2Pt-H_{ads} \rightarrow 2Pt-CO_2 + H_2O + Pt \qquad (3)$$

In order to create alternative, highly efficient, and affordable catalysts for the methanol oxidation reaction, substantial research has been done on enhancing non-platinum-based catalysts for methanol oxidation reaction (MOR).[17] Transition metal catalysts including metal oxides, metal hydrogen sulfide, layered double hydroxide (LDH)[18,19] and Metal–Organic Framework (MOF)[20,21] have recently been investigated as electrocatalysts for DMFCs due to, their availability, low cost, and their exceptional performance in the hydrogen evolution process (HER) and the methanol oxidation reaction (MOR).[22,23] So, the current research worldwide focuses on creating highly effective and affordable low-cost catalyst materials for the oxidation of methanol (MOR) including metal oxide incorporated into carbon material or metal–organic framework (MOF) as a support.[24] To synthesize a Co-MOF and its composites with reduced graphene oxide (rGO) for the electrochemical oxidation of methanol with a current density of 29.1 mA cm^{-2}, Mehek *et al.* used a solvothermal technique.[25] Co-MOF/50% CNTs demonstrated enhanced electrocatalytic activity at a scan rate of 50 mV s^{-1} and a current density of 35 mA cm^{-2} at a voltage of 0.335 V.[26] Furthermore, using the traditional pyrolysis approach, Anchu *et al.* synthesized Co@CNT and evaluated it in the electrochemical oxidation of methanol, revealing a current density of 0.9 mA cm^{-2}.[27] These composites may, however, only exhibit a restricted stability and current density. Until now, transition metal-based electrocatalysts have yet to be thoroughly investigated and reported as a replacement for noble metal-based electrocatalysts in MOR sufficiently with satisfactory results.[28]

Metal–organic frameworks (MOFs) are a new family of crystalline porous materials which is created by coupling metals with secondary building units (SBUs) to organic ligands.[29,30] MOFs have attracted scientific attention due to their high specific surface area, diverse 3D permeability, unsaturated metal centers, symmetrically distributed active sites, good stability, and large pore volume.[31,32] To overcome their relatively low electronic conductivity and chemical instability, MOFs are also often incorporated into conductive materials such as metal compounds, carbonaceous materials, or composites thereof to create functional materials.[33,34] However, due to their controlled and unique properties, they offer (a) potential for synthesizing transition metal oxides (TMOs), as MOFs can be annealed to produce self-templated metal oxides; widely used as a precursor and template. In particular, the hollow/porous and nanosized structure provides more active sites, which develops ionic adsorption. (b) Multi-metallic oxides are easily made from heterometallic MOFs as precursors through calcinations. They have better electrochemical performance than single metal

oxide because of the synergistic interaction of the different metal species and oxidative CO removal from the surface.[35] It is thought that MOFs are a rich source of carbon and nitrogen, and the *in situ*-produced carbon and nitrogen atoms can be kept at the right temperature and environment, which can improve the electrochemical performance and mechanical stability of the produced materials in the anode application.[36,37]

Additionally, compared to Pt, Cu-based electrocatalysts are less susceptible to CO adsorption in an alkaline environment, making them suitable materials for MOR in a fuel cell.[38] However, because copper has a low MOR activity when used alone, so alloying could be used to boost the properties of copper to achieve a specific need that copper cannot meet on its own. Based on the above aspects, nickel is one of the most important non-noble catalysts, and its MOF composites can vary from Ni^{2+} to Ni^{3+}, and *vice versa*, with low cost and anti-poisoning properties.[39–41] Moreover, the cobalt-based MOFs, commonly known as Co-MOF-71, are one of the most active MOFs at MOR.[42] Cobalt is a transition metal that provides redox active sites, has stronger electrochemical activity, and can participate in faradaic redox processes on surfaces.[43] Catalytic applications of Co-MOF-71 in ORR, HER, and OER were successfully evaluated at appropriate current densities.[42,44,45] Bimetallic Metal–Organic Frameworks (MOFs) Cu/Ni-MOFs have two different metal ions at the inorganic nodes.[46] Bimetallic MOF-derived nanomaterials feature exposed active sites, high stability, and electrical conductivity, making them beneficial for use in electrochemical energy storage and conversion, as well as in the catalysis of more difficult processes in harsh environments.[47]

The key to improving the electrocatalytic activity is the coupling effect between mixed metals.[48] Adding a third metal such as Co to bimetallic Cu/Ni MOFs creates a trimetallic MOFs matrix (Cu/Ni/Co MOFs) that changes the coordination environment and electrical properties of the active sites, further increasing their activity.[49] This study aims to develop promising electrode materials with improved electrochemical activity and stability for methanol oxidation reactions. Therefore, various MOFs-based composites and their metal/metal oxide derivatives were prepared by solvothermal approach and deposited on a carbon paste electrode to verify their activity towards methanol oxidation reaction in an alkaline medium (NaOH). The synthesized nanocomposites were denoted as Cu-MOF, Cu/Ni-MOF, and Cu/Ni/Co-MOF. The use of cobalt–nickel (Co–Ni)-based metal–organic frameworks (MOFs) containing inorganic/organic species has been demonstrated to yield high current densities due to their high redox response. The synergistic interactions between different metals and ligands endow these materials with high activity. It exhibits high electrochemical conductivity and an exceptional electrolyte access zone, allowing for a significant number of active sites and fast charge transfer rates.

2. Experiment

2.1. Materials

$Co(NO_3)_2 \cdot 6H_2O$, $Cu(NO_3)_2 \cdot 4H_2O$, $Ni(NO_3)_2 \cdot 6H_2O$, and *N,N*-dimethylformamide (DMF), were purchased from Alpha

Chemika. The organic ligand, 2-aminoterephthalic acid, was purchased from Sigma Aldrich. Piochem provided the sodium hydroxide (NaOH). Alpha Chemistry supplied the methanol (India). For carbon paste, ACROS Organics provided the graphite powder, and Fluka supplied the paraffin oil. All preparations were made using distilled water.

2.2. Preparation of MOF composites

2.2.1 Cu-MOF. A solvothermal procedure was used to synthesize the three composites of MOFs. For Cu-MOF, (3 mmol) 2-aminoterephthalic acid was dissolved in 120 ml N,N-dimethylformamide (DMF), the metal precursors $Cu(NO_3)_2 \cdot 4H_2O$ (3 mmol) was injected to the previous solution. Then, a magnetic stirrer is used to agitate the mixture until it becomes homogeneous. After that, the solution was transferred to a Teflon-lined-stainless steel autoclave, and the solvothermal process was carried out at 160 °C for 12 h, then cooled to ambient temperature. Finally, the mixture was filtered, centrifuged, washed, and dried for 24 h at 60 °C. The resultant material was sintered in the presence of N_2 gas at 600 °C for two hours with a heating rate of 10 °C min^{-1}. The carbonized Cu-MOF was assigned as MOFP1.

2.2.2 Cu/Ni-MOF and Cu/Ni/Co-MOF. For Cu/Ni-MOF, and Cu/Ni/Co-MOF they were prepared by the same described previous method for the preparation of Cu-MOF with the difference in the concentration of the metal salt precursor. In Cu/Ni-MOF, $Cu(NO_3)_2 \cdot 4H_2O$ (1.5 mmol), $Ni(NO_3)_2 \cdot 6H_2O$ (1.5 mmol) were used. In Cu/Ni/Co-MOF, the precursors were $Co(NO_3)_2 \cdot 6H_2O$ (2 mmol), $Cu(NO_3)_2 \cdot 4H_2O$ (0.5 mmol), $Ni(NO_3)_2 \cdot 6H_2O$ (0.5 mmol). All solutions were injected into the prepared solution of 2-aminoterephthalic acid (3 mmol) that dissolved in 120 ml N,N-dimethylformamide (DMF). Then, proceeding the solvothermal reaction and carbonization treatment as described previously in Section 2.2.1. The carbonized Cu/Ni-MOF and In Cu/Ni/Co-MOF were assigned as MOFP2 and MOFP3, respectively (Scheme 1).

2.3. Characterization

XRD analysis was performed using an X-ray diffractometer (Cu-Kα radiation) operating at a voltage of 40 kV and a current of 35 mA. The Fourier Transform Infra-red spectroscopy (FTIR) characterization was carried out using a Bruker Vertex 70. The structural morphology was checked by Scanning Electron Microscopy (SEM, ZEISS, Sigma 500 VP). The energy-dispersive X-ray spectroscopy (EDX) was used to identify the elemental composition (EDX; EDAX AMETEK analyzer). The surface area and porosity were investigated from the N_2 adsorption data using a Tri-Star II 3020 (Micromeritics, USA) analyzer by the Brunauer–Emmett–Teller (BET) method. The hydrodynamic particle sizes and zeta potential were measured using Malvern zeta sizer equipment (Malvern Instruments Ltd).

2.4. Working electrode fabrication

The electrode was fabricated by mixing 150 µL of paraffin oil and 1 g of graphite powder in a mortar and pestle for 30 minutes, then the mixture was dried for 30 minutes. A Teflon tube served as a holder for the finished paste, and a copper wire served as the electrical contact. Before use, the electrode surface was polished on a smooth piece of paper and then cleaned with double-distilled water.[50] The prepared electrocatalyst was then dissolved in 200 µL of isopropanol and 20 µL of 5% Nafion solution. The mixture was then sonicated at room temperature for one hour. Finally, 20 µL of the sonicated suspension was poured over the active area of the carbon paste electrode and dried at 60 °C for 15 min.

2.5. Electrocatalytic activity measurements

The electrochemical tests were performed using three-electrodes glass electrochemical cell with the carbon paste as the working electrode, graphite as the counter electrode, and Ag/AgCl as the reference electrode. The measurements were conducted using NOVA 1.11 Potentiostat/Galvanostat
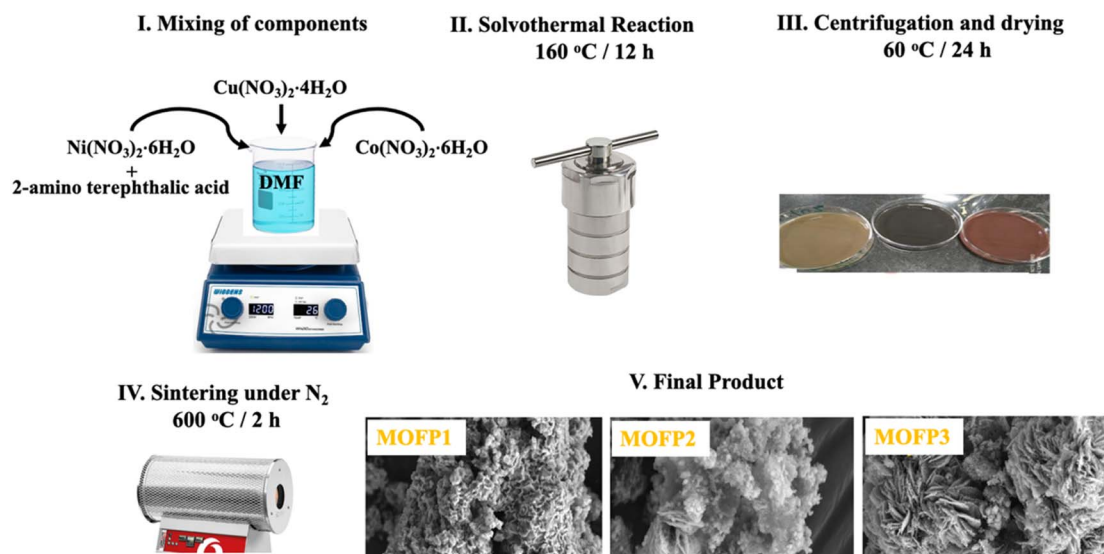
Scheme 1 Schematic of the synthetic process for the derived MOF composites.

(AUTOLAB PGSTAT 302N, Metrohm, Herisau, Switzerland) software. An alkaline electrolyte of 1.0 M NaOH was used to investigate the electrocatalytic activity of the manufactured electrodes in the presence and absence of various methanol concentrations. The used electrochemical tests were cyclic voltammetry at different scan rates between 5–60 mV s^{-1} within a potential range of −0.1–0.7 V. Moreover, the chronoamperometry (CA) tests were recorded at 0.7 V for 1 h.

2.6. The evaluation of main electrochemical parameters (b, j_o, C_{dl}, ESCA) for samples MOFP1, MOFP2 and MOFP3

Tafel plots obtained by fitting the polarisation curves as overpotential *versus* log current density: $\eta = a + b \log[j]$, where η is the overpotential, j is the current density, and b is the Tafel slope. Tafel plots are obtained by fitting in the linear region of Tafel curve. The Tafel curve's intersection in the linear extension zone is the exchange current density (j_o). The double layer capacitance (C_{dl}) and electrochemically active surface area (ECSA) of samples evaluated through the CV measurements at different scan rates at the potential window (0–0.1 V) where no faradaic processes took place was used. (C_{dl}) was determined from a CV using the equation: $C_{dl} = \Delta j(j_a - j_c)/2$, where j_a and j_c are anodic and cathodic current densities. Plotting the average current densities *versus* scan rate yielded a straight line with a slope equal to (C_{dl}). The electrochemically active surface area (ECSA) was estimated according to the equation: ECSA = C_{dl}/C_s, where C_s is the specific capacitance of the electrode and was taken as 0.04 mF cm^{-2} in 1 M KOH electrolyte.

3. Results and discussion

3.1. Physicochemical characteristics

The crystalline structure of the prepared MOF composites and their derived oxides were characterized by the X-ray diffraction (XRD), Fig. 1. Fig. 1a, shows the X-ray diffraction pattern of Cu-MOF material. The main peaks centered at 2θ of 10.2°, 17°, 21°, 24.8°, 43°, 50.5°, 74.8° are assigned to the (200), (220), (222), (400), (422), (511), and (751) planes of Cu-MOF composite.[51] The XRD pattern of the derived CuO NPs (MOFP1) is shown in Fig. 1b. The most significant peaks are seen at 2θ of 35.7°, 36.4°, 38.6°, and 42.7°, respectively, which correspond to the crystal planes of (110), (002), (111), and (020) (JCPDS card no. 00-041-0254).[52,53] Fig. 1c, displays the XRD pattern of the as synthesized Cu/Ni-MOF. The Ni-MOF characteristic peaks appears at 2θ of 16.68°(101), 19.65°(200), 34°(022), 44.3°(512), and 50.50°(226), which corresponds to the typical JCPDS no. 00-045-1691 card.[54] In Fig. 1d, the diffraction peaks of NiO at 2θ of 37.20°, 43.20°, 62.87°, and 75.20° are assigned to the (111), (200), (220) and (311) crystal planes, respectively.[55] Fig. 1e, shows the XRD pattern for Cu/Ni/Co-MOF in which the characteristic diffraction planes of Co-MOF are appeared at 2θ of 11.56°, 16.9°, 17.91°, 19.6°, 20.63°, 21.86°, 28.62°, 29.03°, and 43.35°, demonstrating the successful integration of Co into Cu/Ni-MOF.[56] Fig. 1f, shows the characteristic peaks of CoO 2θ of 36.9°, 42.85°, and 64.8° which are assigned to the diffraction planes (311), (400) and (441).[57] These (*hkl*) planes are properly
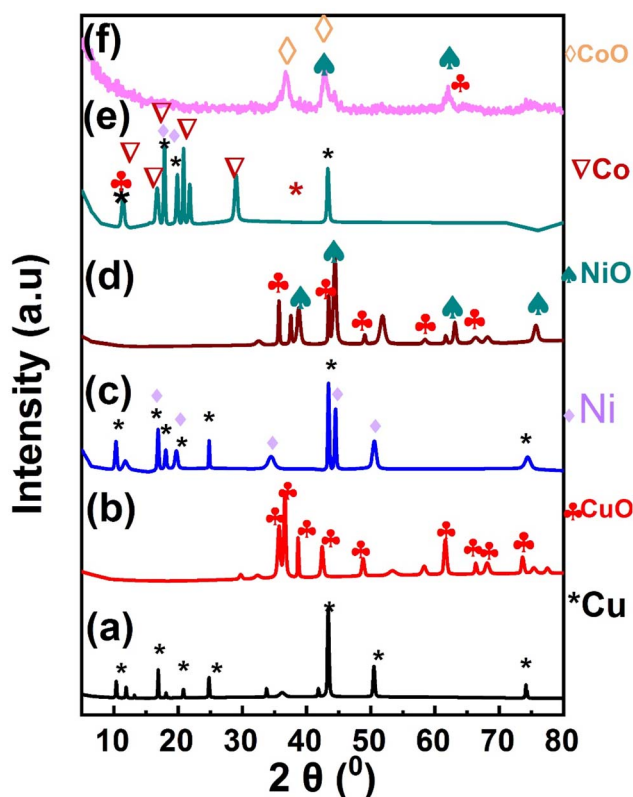

Fig. 1 X-ray diffraction pattern of (a) Cu-MOF, (b) MOFP1, (c) Cu/Ni-MOF, (d) (MOFP2), (e) Cu/Ni/Co-MOF, (f) (MOFP3).

configured with normal JCPDS data card number (80-1538).[42,58] After calcination of MOF, there are absence of peaks related to the derived carbon from MOFs which confirm the formation of amorphous carbon. Previous studies showed that amorphous carbon electrode compared to their crystalline equivalent, allow for additional ion diffusion paths, which would improve electrochemical performance.[59]

The FTIR spectrum in Fig. 2a shows the disappearance of the stretching peak of –OH in Cu MOF revealing the coordination bond between Cu^{2+} and –COOH of 2-aminoterephthalic acid.[60] The amino group of 2-aminoterephthalic acid shows two stretching peaks at 3508 cm^{-1} and 3394 cm^{-1}, while the peak of Cu-MOF was at 3352 cm^{-1} and 3466 cm^{-1} due to the formation of intra-framework hydroxyl group between the amine group and the electron-donating oxygen of the carboxyl group.[61] The Cu-MOF was annealed at 600 °C (MOFP1), as shown in the FTIR spectrum in Fig. 2b. The adsorbed water molecules were responsible for the broad absorption peak at about 3422 cm^{-1}.[62] The OH stretching range is 2700 to 3750 cm^{-1}. The symmetrical Cu–O stretching can be represented by the peak at 1638 cm^{-1}.[63] The vibrational modes of CuO NPs in the range of 500–700 cm^{-1} are revealed by two infrared absorption peaks. The peaks at 512 cm^{-1} and 618 cm^{-1}, reveal the formation of CuO NPs.

The functional groups and metal bonds of Cu/Ni-MOF and Cu/NiO (MOFP2) were investigated by FTIR (Fig. 2c and d). All the prepared catalysts exhibit symmetric and asymmetric C=O stretching as indicated by sharp peaks at 1576 cm^{-1} and
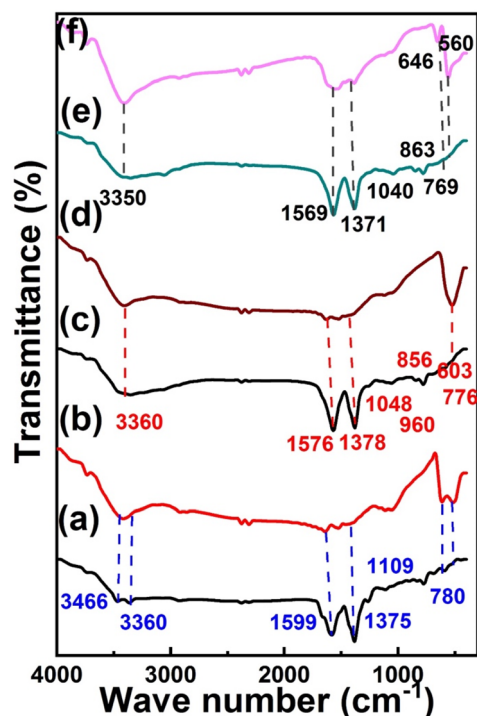
Fig. 2   FT-IR spectrum of (a) Cu-MOF, (d) (MOFP1), (b) Cu/Ni-MOF, (e) MOFP2, (c) Cu/Ni/Co-MOF, (f) (MOFP3).

1378 cm^{-1}, respectively.[64] Due to the removal of protons from the –COOH group of benzenedicarboxylic acid, there is no significant absorption peak at approximately 1715–1680 cm^{-1}.[64] The presence of C–O band at 1576–1048 cm^{-1} indicates that the dicarboxylic acid is coordinated with Ni and Cu.[65] Furthermore, the band at 603 cm^{-1} indicates the formation of metallic bonds with carboxyl groups. At about 3400–3500 cm^{-1}, there is a broad band caused by O–H stretching, confirming that this is a regulated water source connected within the Ni/Cu MOF.[66] According to the FTIR spectrum in Fig. 2d, (Ni/Cu MOF annealed at 600 °C), the bands of the Ni main MOF include O–H stretching: broadband: 3422 cm^{-1} and C–H stretching: 2938 cm^{-1} (stretching: narrowband). In the region of 600–700 cm^{-1}, there is a large absorption band associated with the Ni–O stretching mode. The size of the absorption bands indicates that the NiO particles are nanocrystalline.[55] The jagged absorption bands in the range 1000–1500 cm^{-1} are caused by symmetric and asymmetric O–C=O stretching vibrations and C–O stretching vibrations. The FTIR spectra of Cu/Ni/Co MOF and MOFP3 are shown in Fig. 2e and f. In Fig. 2e, it was observed that asymmetry and symmetry exist in the vibrational band of the H–N group in the range of 3300–3000 cm^{-1}. Additionally, the C–H bending vibrations were assigned to bands at 1058 and 787 cm^{-1},[67] both in-plane and out-of-plane. The v-skeletal resonance (C=C) of the benzene ring was identified as the source of the absorption band at 1566 cm^{-1}.[68–70] The prominent peaks at 1566 and 1382 cm^{-1} were due to symmetric and asymmetric carbonyl bending vibrations.[71] The stretching mode of water (OH) is associated with a broad band of 3405 cm^{-1}. The

presence of the O–H stretching mode indicates that the unchanged MOF is hydrated.[72] The vibrational mode of the Cu–O bond is characterized by the band at 566 cm^{-1}.[73] Fig. 2f shows the CoO features with two distinct bands at 646 and 560 cm^{-1}.[74] The interactions between the Cu, Ni, Co, and NH groups throughout the composite process are the basis for all modifications, which support the idea of preparation of Cu/Ni/Co-MOF.

Fig. 3a and b of Cu-MOF after carbonization (MOFP1) shows well homogenized, spherical, nanoparticle aggregates forming a rough porous structure.[75] Fig. 3c–e, shows the morphology of Cu/Ni-MOF after carbonization (MOFP2). The combination of homogenous spherical particles of CuO and hollow shell structure of NiO are visible in the SEM micrographs and appear as open flower structures that might enhance its electrochemical characteristics Fig. 3d. The FESEM images of Co/Cu/Ni MOF after carbonization (MOFP3) are shown in Fig. 3f–h. It is characterized by a sharp, thin coating aggregated flakes, up to 300 nm in size. Fig. 3h, appears as an overall spherical cluster, consistent with the morphology described in previous work.[69] This indicates that the porous CoO microspheres maintain the shape of the precursor. The accumulation of small particles forms rich pores, which proves that pores are formed during calcination. Several overlapping nanospheres were present and began to form groups similar to pagodas or cauliflowers. The results show properties of both nano- and microsized components, such as shortened transport paths and enhanced tap density, which are beneficial for improving methanol oxidation.[76] Furthermore, the cavity between the formed nanoparticles allows for the effective penetration of electrolyte.[77] As shown in Fig. S1a and b† TEM and HRTEM image for MOFP2 is providing evidence of their spherical particles combined with hollow shell structures.

In Fig. 5a, the energy dispersive X-ray spectroscopy (EDX) confirms the presence of copper, oxygen, and carbon atoms for (MOFP1). Furthermore, the EDX of MOFP2, Fig. 5b, shows the presence of copper, nickel, carbon, and oxygen which confirms the successful integration of Ni with Cu-MOF. Additionally, Fig. 5c, represent the EDX analysis for MOFP3 where cobalt, copper, nickel, oxygen, and carbon atoms are found in Table S1.†

The porous structure of the prepared MOFs was investigated using N_2 adsorption–desorption measurements in Fig. 4d. According to the IUPAC classification scheme, the adsorption isotherms for all those materials are combinations of types I and IV, which suggests the development of the mesopore structures. Table 1, shows the average pore radius (nm) (BJH method) and the BET surface area of the MOFP composites. The MOFP2 possesses the highest BET surface area of (21 m^2 g^{-1}) compared to other fabricated MOFP composites, together with its average pore size of 4.5 nm can improve methanol transport and its oxidation through the porous material.

3.2. Oxidation of methanol

3.2.1 Electrochemical activity. The electrocatalytic activity of the MOFs composites modified working electrode in 1 M NaOH with and without 1 M methanol was investigated using
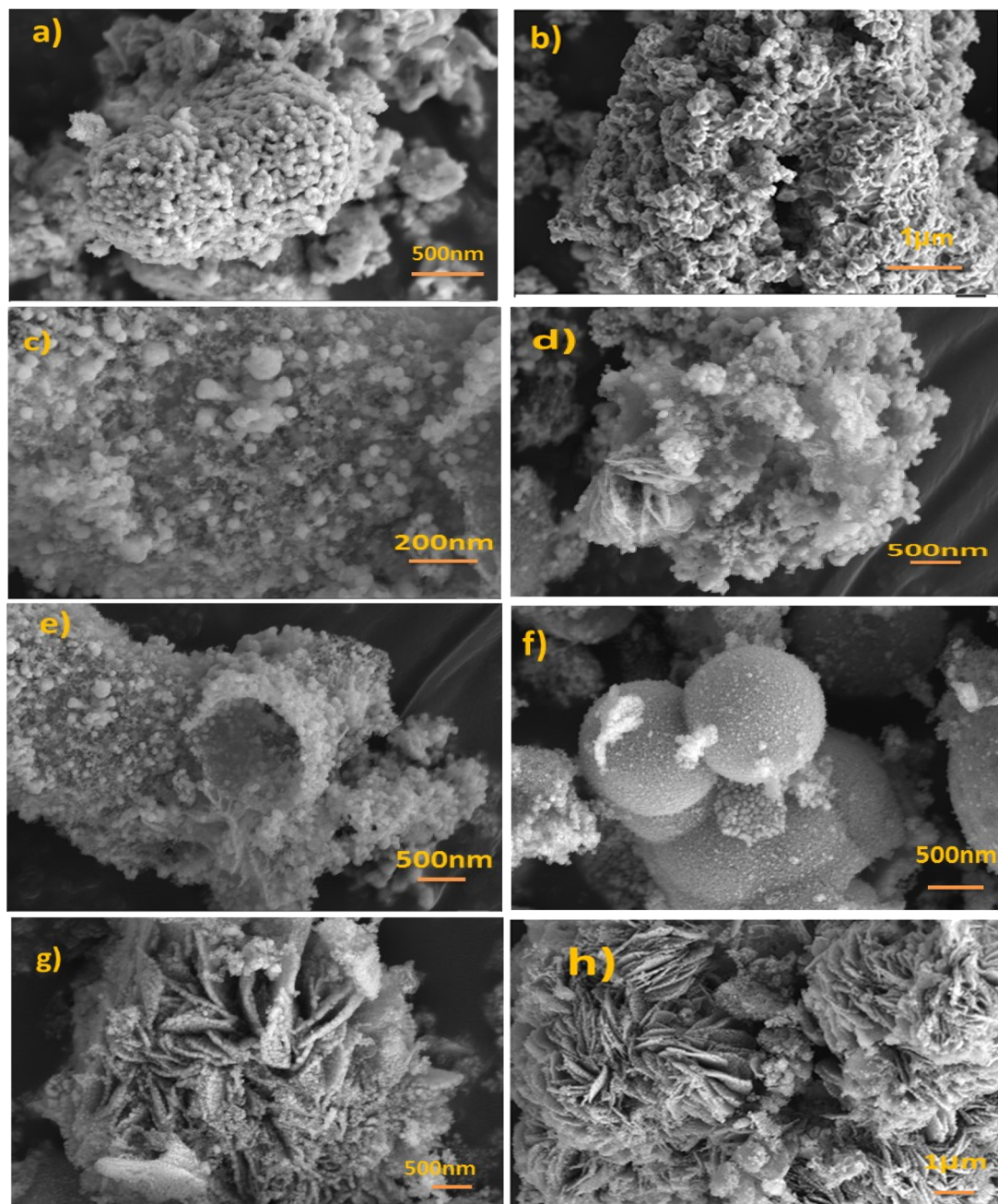
Fig. 3 FE-SEM images (a and b) for MOFP1, (c–e) for MOFP2, and (f–h) for MOFP3 at different magnification scales.

cyclic voltammetry technique in a potential window of −0.1 to 0.7 V (vs. Ag/AgCl) at room temperature and at different scan rates (5, 10, 20, 30, 40, 50 and 60 mV s^{-1}), Fig. 5. A comparison between the electrochemical activity of MOFP1, MOFP2, and MOFP3 in 1 M NaOH is shown in Fig. 5a. From Fig. 5a, higher electrochemical activity was observed for MOFP2, while MOFP1 and MOFP3 have comparable activity. With the addition of methanol (1 M), an increase in the current density was noticed, indicating that these materials have activity to methanol oxidation, Fig. 5b. In addition, the MOFP2 has the highest current density of 38.98 mA cm^{-2} at a scan rate of 60 mV s^{-1} meaning that it has the best activity for methanol oxidation.

Fig. 5b–g, shows the change of the current density with the applied scan rate for all composites before and after calcination. As expected, the peak current density increases linearly as the sweep rate increases from 0 to 60 mV s^{-1}, indicating that the methanol oxidation process is kinetically controlled process, Table 2. The increase in the electrocatalytic activity of MOFP2 can be attributed to the synergistic effect of its constituents of copper, nickel and 2-aminoterephthalic acid which develop the pores inside the structure of the catalyst framework, improving the surface area which has a positive contribution on the catalyst activity, Table 1. Moreover, the nanoflower structure may contribute to better diffusion for the electrolytic ions and better
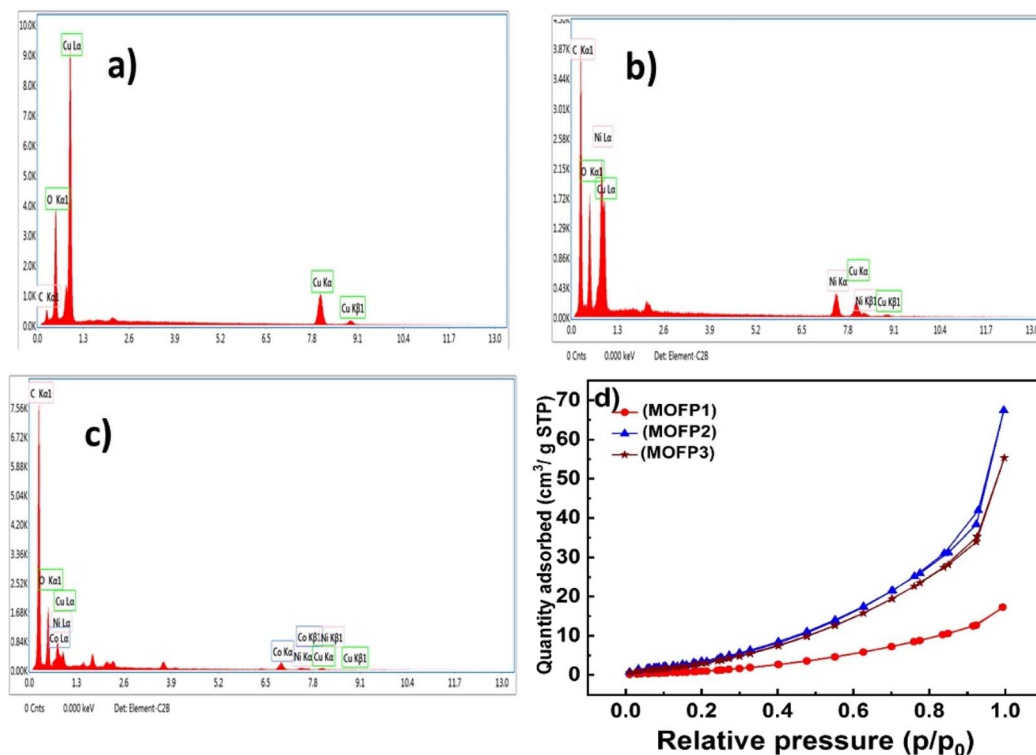
Fig. 4 EDX of (a) MOFP1, (b) MOFP2, (c) MOFP3, (d) nitrogen adsorption/desorption isotherms of MOFs.

methanol adsorption.[78] The intrusion between three metals in MOFP3 and one metal in MOFP1 prevented the active catalytic sites from carrying out the reaction at low potential values, resulting in charge transfer at high potentials.[79] Agglomeration is generally a serious problem for electrocatalytic materials because agglomeration reduces the number of active sites for electrocatalytic reactions and thus reduces the performance which can be a reason for reducing the activity of MOFP3. Therefore, special techniques are needed to prevent or minimize the agglomeration process to increase the surface area of the catalyst and improve its performance.[80] Another reason for high current density for MOFP2 than others is the crystal size as observed before in XRD description.[81] As shown in Table 3, our modified electrode MOFP2 exhibits higher electrocatalytic activity than previously reported electrocatalytic activity for methanol electrooxidation. The onset potentials were measured for MOFP1, MOFP2 and MOFP3 toward methanol oxidation in alkaline media through CVs as shown in Fig. S2.† As shown in Fig. S2,† the CV curves of the different samples in 1 M NaOH with 1 M methanol were measured. As well as the associations of the onset potential and the current density with the different MOFPs, the onset potentials were found to be 0.14, 0.05 and 0.2 V (*vs.* Ag/AgCl), respectively. The MOFP2 exhibited a strong oxidation current density (35 mA cm^{-2}) in the presence of 1 M methanol, and a relatively low onset potential of methanol oxidation, which was 0.05 V, such that the MOFP2 needed low energy for the redox reactions to occur. The square root of the potential scan rate and the forward peak current density of MOFP1, MOFP2 and MOFP3 displayed in Fig. S3(a).† The anodic and cathodic peak intensities rose linearly with the

square root of the potential scan rate in all cases. Straight lines with correlation factors that were nearly equal to unity were discovered in each case. This illustrates how methanol or its byproducts permeate into the pores of the MOFPs. MOFP2 has a larger line slope than the MOFP1 and MOFP3. This variation in the slope indicates increased activity, which is linked to a change in electrocatalysis capacity.[82] The greater the dispersion, the steeper the slope.[83] The Tafel graphs, which contrast current density with over potential to assess the reaction kinetics of catalytic development, are shown in Fig. S3(b).† The formula $E - E_o$ is used to determine over potential.[84] Table S2† shows the Tafel slopes (at potential of 0.7 V) that were computed for the examination of catalytic process reaction kinetics. The slopes values at lower potential would indicate that the initial electron transfers and C–H bond breaks in methanol, which characterizes the rate-determining step.[85] MOFP2 make feasible the accessibility of reactant toward electrode surface and exhibited greater activity for the methanol oxidation than MOFP1 and MOFP3. The exchange current density of MOFP1 is 0.01, FOR MOFP2 is 0.08 and for MOFP3 is 0.06 mA cm^{-2}. The electrochemical double-layer capacitance (C_{dl}) was used to estimate the electrochemically active surface areas (ECSA) based on the CVs obtained at various scan rates in the non-faradaic range of possibilities 0–0.1 V *vs.* Ag/AgCl.[86] A straight line with a slope equal to C_{dl} was produced when the capacitance current (I_c) was plotted against the scan rate (v). ECSA was computed by dividing C_{dl} by C_s, the specific capacitance.[87]
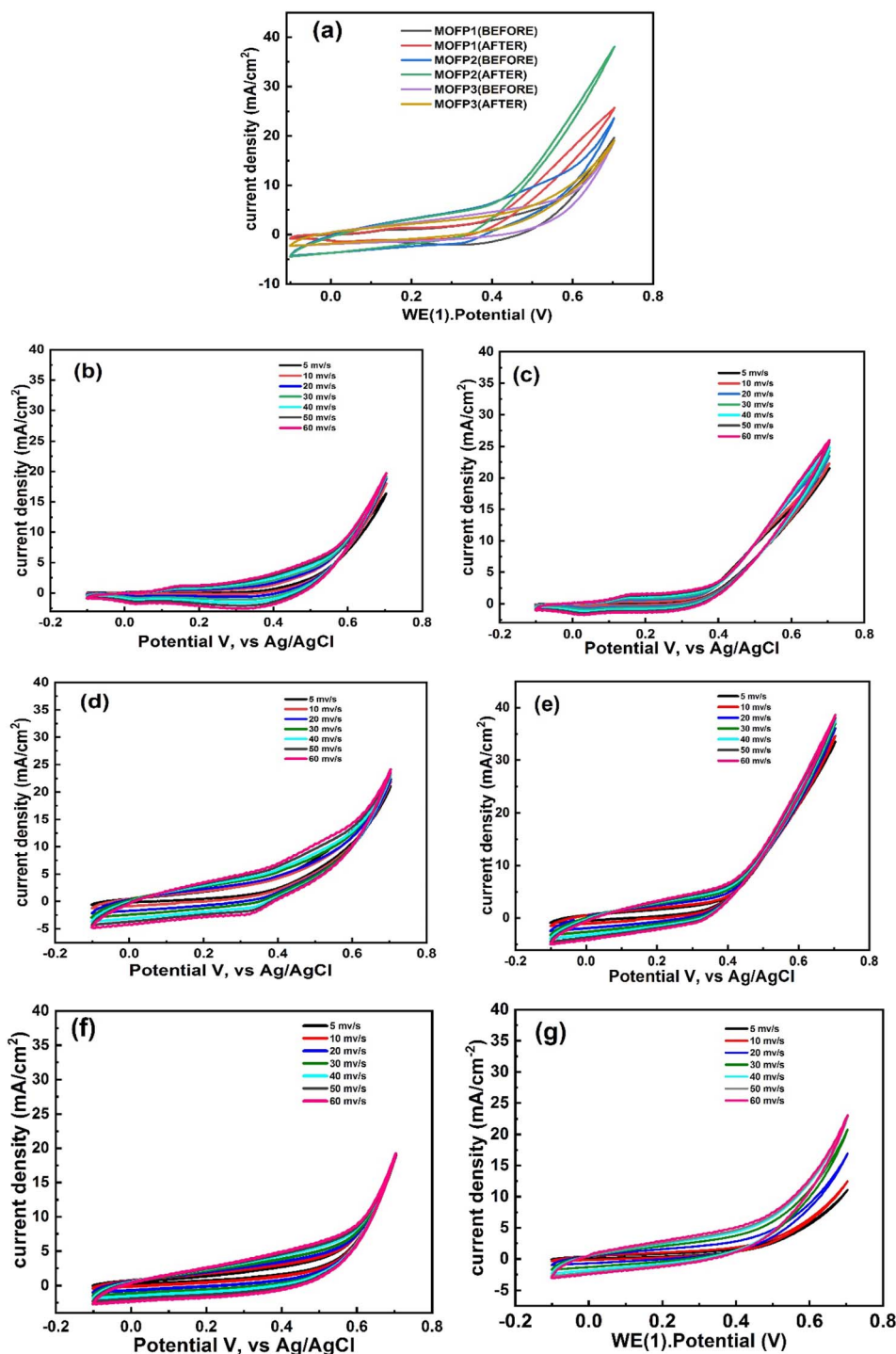
$$ECSA = C_{dl}/C_s \qquad (4)$$

Fig. 5 Cyclic voltammograms, CV of (a and b) MOFP composites without methanol and after addition of 1 M methanol, respectively at 50 mV s^{-1}, CV at different scan rates without methanol and after addition of 1 M methanol, respectively (b and c) MOFP1, (d and e) MOFP2, (f and g) MOFP3.

Table 1 Surface area analysis of MOF composites

Sample	S_{BET} (m^2 g^{-1})	$L_{o(BJH)}$ (nm)
MOFP1	7	14.9
MOFP2	21	4.5
MOFP3	19	4.4

where C_s is 0.04 mF cm^{-2} based on values reported for metal electrodes in aqueous NaOH solution.[88] As Fig. S4† for MOFPs in 1.0 M KOH solution, the calculated value of C_{dl} for MOFP1, MOFP2 and MOFP3 0.00456, 0.01241 and 0.00121 mF cm^{-2}, and as mentioned in Table S2.† ECSA was for MOFP1, MOFP2 and MOFP3 114, 310.25 and 30.5 cm^{-2} respectively. According to the results of ECSA for three materials, MOFP2 has the

Table 2 The current densities of the MOFP1, MOFP2 and MOFP3 samples at different scan rates in 1 M NaOH

Scan rate (mV s^{-1})	Current density of MOFP1 (mA cm^{-2})	Current density of MOFP2 (mA cm^{-2})	Current density of MOFP3 (mA cm^{-2})
5	18.97	21.17	16.38
10	19.19	21.77	18.07
20	19.20	22.32	18.73
30	19.22	22.90	19.14
40	19.25	22.99	19.61
50	19.26	23.45	19.65
60	19.27	24.10	19.74

Table 3 Comparison of current densities, electrolyte, and applied potential with several reported electrocatalysts for methanol oxidation

Electrocatalyst	Electrolyte	Applied voltage	Current density (mA cm^{-2})	Ref.
Ni-MOF/IL	0.5 M NaOH	0.5 V (*vs.* SCE)	18	**89**
MOF-74	0.1 M NaOH	0.7 V (*vs.* Ag/AgCl)	13.46	**90**
20% Ni/MIL-110	0.1 M NaOH	0.7 V (*vs.* Ag/AgCl)	14.40	91
C–Pt-ZIF-8e	0.5 M KOH	—	16.16	92
MOFP1	1.0 M NaOH	0.7 V (*vs.* Ag/AgCl)	23.23	**This work**
MOFP2	1.0 M NaOH	0.7 V (*vs.* Ag/AgCl)	38.98	**This work**
MOFP3	1.0 M NaOH	0.7 V (*vs.* Ag/AgCl)	26.04	**This work**

highest ECSA with high available active sites for methanol oxidation.

3.2.2 Electrode stability. The stability of the synthesized catalysts was evaluated using a chronoamperometry test. The measurements were carried out in 1 M methanol and 1 M NaOH, keeping the voltage constant at 0.7 V for 1 h using three-electrode setup. Fig. 6, compares the relative stability of MOF composites. MOFP2 has the best electrocatalytic activity for MOR with enhanced stability than MOFP1 or MOFP3. As appeared, the current gradually decreases over time till reaches a quasi-steady state after 3600 s. This may be because the catalytic sites were initially covered with methanol.[93,94] However,

as the reaction progresses, an equilibrium layer of methanol forms, which slows down the entire process and affects the stability of any electrocatalysts produced. This test suggests that all the prepared composites MOFP1, MOFP2, and MOFP3 have excellent long-term stability. As shown in Fig. S5a and b,† TEM and HRTEM images proved the stability and morphological retention of MOFP2 after methanol oxidation reaction. Fig. S5b† it confirmed the presence of, Ni oxide with the *d*-space value of 0.21, 0.24, corresponding to (111) and (200) plane of the NiO, and *d*-space value of 0.23 and 0.25 nm which related to the (111) and (002) plane of CuO, respectively, which corroborates the XRD test results.[95] This result proven the stability of the material and preserved structure as before the methanol oxidation reaction. As shown in Fig. S6,† it confirmed that the sample (MOFP2) after 1500 cycles has high activity and has the current density = 34.71 mA cm^{-2} retention percent of 89.5%.
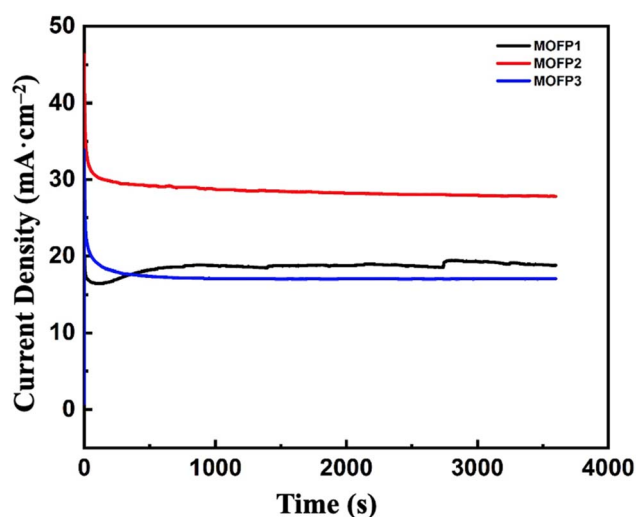
4. Conclusions

A cost-effective and environmentally friendly solvothermal process was used to fabricate the MOFs composites and anneal at 600 °C in a N$_2$ flow to obtain their corresponding derived metal oxides. By using this preparation method, nanoflowers or nanoflakes of MOFs derived metal oxides can be produced. Our study shows that the synthesized catalyst has a very high potential to be used in direct methanol fuel cells. The ability of the materials to catalyze the methanol oxidation reaction was investigated. The MOFP2 composite showed the best performance with a maximum current density of 38.98 mA cm^{-2} at a scan rate of 60 mV s^{-1}. The surprising combination of acceptable high current density and affordable price makes it a potential replacement for expensive electrocatalysts in various fuel cell applications.

Fig. 6 Chronoamperometric curves of MOFP composites in 1 M methanol and 1 M NaOH at 60 mV s^{-1} and a fixed potential of 0.7 V.

Data availability

The authors confirm that the data supporting the findings of this study are available within the article and its ESI.†

Author contributions

W. Kamal: writing, results, discussion, and experiments. Rehab Mahmoud: review, editing, supervision and project administration. Abeer Enaiet Allah: review and supervision. Abdalla Abdelwahab: data analysis, editing, supervision. Ahmed A. Farghali: review, supervision and project administration.

Conflicts of interest

The authors certify that they are aware of no financial conflicts of interest or close personal relationships that could interfere with the research described in this publication.

References

1 H. F. M. Mohamed, E. E. Abdel-Hady, M. F. M. Hmamm, M. Ibrahim, H. Ahmed, M. Mondy and H. Yehia, *IOP Conf. Ser.: Mater. Sci. Eng.*, 2018, **464**(1), 012002.

2 M. Lo Faro, V. Antonucci, P. L. Antonucci and A. S. Aricó, *Fuel*, 2012, **102**, 554–559.

3 G. Cacciola, V. Antonucci and S. Freni, *J. Power Sources*, 2001, **100**(1), 67–79.

4 T. Eisa, H. O. Mohamed, Y. J. Choi, S. G. Park, R. Ali, M. A. Abdelkareem, S. E. Oh and K. J. Chae, *Int. J. Hydrogen Energy*, 2020, **45**, 5948–5959.

5 Y. S. Li, T. S. Zhao and Z. X. Liang, *J. Power Sources*, 2009, **190**, 223–229.

6 J. Taraszewska and G. Rosłonek, *J. Electroanal. Chem.*, 1994, **364**, 209–213.

7 W. Tu, Y. Sun, D. Wu, H. Wang, H. Huang, M. Shao, Y. Liu and Z. Kang, *Mater. Chem. Phys.*, 2019, **225**, 64–71.

8 B. Y. Xia, J. N. Wang and X. X. Wang, *J. Phys. Chem. C*, 2009, **113**, 18115–18120.

9 H. A. Gasteiger, S. S. Kocha, B. Sompalli and F. T. Wagner, *Appl. Catal., B*, 2005, **56**, 9–35.

10 A. Nouralishahi, Y. Mortazavi, A. A. Khodadadi, M. Choolaei, L. T. Thompson and B. A. Horri, *Appl. Surf. Sci.*, 2019, **467–468**, 335–344.

11 H. Liu, C. Song, L. Zhang, J. Zhang, H. Wang and D. P. Wilkinson, *J. Power Sources*, 2006, **155**, 95–110.

12 S. Guo, S. Zhang and S. Sun, *Angew. Chem., Int. Ed.*, 2013, **52**, 8526–8544.

13 E. E. Abdel-Hady, M. Shaban, M. O. Abdel-Hamed, A. Gamal, H. Yehia and A. M. Ahmed, *Nanomaterials*, 2022, **3**, DOI: **10.3390/nano12030492**.

14 C. Y. Du, T. S. Zhao and W. W. Yang, *Electrochim. Acta*, 2007, **52**, 5266–5271.

15 T. Seiler, E. R. Savinova, K. A. Friedrich and U. Stimming, *Electrochim. Acta*, 2004, **49**, 3927–3936.

16 M. Mansor, S. N. Timmiati, W. Y. Wong, A. M. Zainoodin, K. L. Lim and S. K. Kamarudin, *Catalysts*, 2020, **10**, 1–20.

17 Y. Liu, B. Hu, S. Wu, M. Wang, Z. Zhang, B. Cui, L. He and M. Du, *Appl. Catal., B*, 2019, **258**, 117970.

18 E. E. Abdel-Hady, R. Mahmoud, S. H. M. Hafez and H. F. M. Mohamed, *J. Mater. Res. Technol.*, 2022, **17**, 1922–1941.

19 K. Patil, P. Babar, D. M. Lee, V. Karade, E. Jo, S. Korade and J. H. Kim, *Sustainable Energy Fuels*, 2020, **4**, 5254–5263.

20 R. Mehek, N. Iqbal, T. Noor, H. Nasir, Y. Mehmood and S. Ahmed, *Electrochim. Acta*, 2017, **255**, 195–204.

21 R. K. Tripathy, A. K. Samantara and J. N. Behera, *Dalton Trans.*, 2019, **48**, 10557–10564.

22 J. Wang, X. Cao, L. Fang, X. You, K. Wong, S. Cao, C. Xiao, S. Cai, Y. Huang, X. Zhang and Z. Chen, *Int. J. Hydrogen Energy*, 2019, **44**, 16411–16423.

23 L. Qian, S. Luo, L. Wu, X. Hu, W. Chen and X. Wang, *Appl. Surf. Sci.*, 2020, **503**, 144306.

24 Z. Jia, Y. Wang and T. Qi, *RSC Adv.*, 2015, **5**, 62142–62148.

25 R. Mehek, N. Iqbal, T. Noor, H. Nasir, Y. Mehmood and S. Ahmed, *Electrochim. Acta*, 2017, **255**, 195–204.

26 A. A. Kotp, A. Abdelwahab, A. A. Farghali, W. M. A. E. Rouby and A. Enaiet Allah, *RSC Adv.*, 2023, **13**, 27934–27945.

27 A. Ashok, A. Kumar, A. Yuda and A. Al Ashraf, *Int. J. Hydrogen Energy*, 2022, **47**(5), 3346–3357.

28 M. M. Rajpure, H. S. Jadhav and H. Kim, *Colloids Surf., A*, 2022, **654**, 130062.

29 H. A. Younes, M. Taha, R. Khaled, H. M. Mahmoud and R. M. Abdelhameed, *J. Alloys Compd.*, 2023, **930**, 167322.

30 H. Furukawa, K. E. Cordova, M. O'Keeffe and O. M. Yaghi, *Science*, 2013, 341.

31 J. Lee, O. K. Farha, J. Roberts, K. A. Scheidt, S. T. Nguyen and J. T. Hupp, *Chem. Soc. Rev.*, 2009, **38**, 1450–1459.

32 Y. Ri Lee, M. Tian, S.-N. Kim, W.-S. Ahn and K. Ho Row, *Adsorpt. Sci. Technol.*, 2014, **32**(9), 725–735.

33 X. Li, S. Zheng, L. Jin, Y. Li, P. Geng, H. Xue, H. Pang and Q. Xu, *Adv. Energy Mater.*, 2018, **8**, 1800716.

34 L. Yaqoob, T. Noor, N. Iqbal, H. Nasir and A. Mumtaz, *Sci. Rep.*, 2021, **11**(1), 13402.

35 X. Tan, X. Wu, X. Lin, A. Zeb, X. Xu, Y. Luo and J. Liu, *Inorg. Chem. Front.*, 2020, **7**, 4939–4955.

36 G. S. Day, J. Li, E. A. Joseph, P. C. Metz, Z. Perry, M. R. Ryder, K. Page and H. C. Zhou, *Nanoscale Adv.*, 2020, **2**, 2758–2767.

37 X. Cui, W. Guo, M. Zhou, Y. Yang, Y. Li, P. Xiao, Y. Zhang and X. Zhang, *ACS Appl. Mater. Interfaces*, 2015, **7**, 493–503.

38 I. Danaee, M. Jafarian, F. Forouzandeh, F. Gobal and M. G. Mahjani, *Int. J. Hydrogen Energy*, 2008, **33**, 4367–4376.

39 M. Mansor, S. N. Timmiati, K. L. Lim, W. Y. Wong, S. K. Kamarudin and N. H. Nazirah Kamarudin, *Int. J. Hydrogen Energy*, 2019, **44**, 14744–14769.

40 X. Wang, S. Xi, W. S. V. Lee, P. Huang, P. Cui, L. Zhao, W. Hao, X. Zhao, Z. Wang, H. Wu, H. Wang, C. Diao, A. Borgna, Y. Du, Z. G. Yu, S. Pennycook and J. Xue, *Nat. Commun.*, 2020, **11**, 1–9.

41 M. Jahan, Z. Liu and K. P. Loh, *Adv. Funct. Mater.*, 2013, **23**, 5363–5372.

42 C. H. Jadhav, K. B. Pisal, A. R. Chavan, S. M. Patil, P. B. Patil and P. K. Pagare, *Mater. Today: Proc.*, 2020, **43**, 2742–2746.

43 L. Yaqoob, T. Noor and N. Iqbal, *Int. J. Energy Res.*, 2021, **45**, 6550–6583.

44 E. Loni, A. Shokuhfar and M. H. Siadati, *Catal. Surv. Asia*, 2021, **25**, 114–147.

45 R. Ojani, J. Bakhsh, A. Ahmady and S. Reza, *Caspian J. Chem.*, 2013, **2**, 45–57.

46 L. Chen, H. F. Wang, C. Li and Q. Xu, *Chem. Sci.*, 2020, **11**, 5369–5403.

47 H. Wang, Q. L. Zhu, R. Zou and Q. Xu, *Chem*, 2017, **2**, 52–80.

48 K. Zhang, W. Guo, Z. Liang and R. Zou, *Sci. China: Chem.*, 2019, **62**, 417–429.

49 D. Senthil Raja, C. L. Huang, Y. A. Chen, Y. M. Choi and S. Y. Lu, *Appl. Catal., B*, 2020, **279**, 119375.

50 R. H. Mahmoud, F. A. Samhan, M. K. Ibrahim, G. H. Ali and R. Y. A. Hassan, *Bioprocess Biosyst. Eng.*, 2021, **44**, 759–768.

51 S. M. Hwang, S. Y. Choi, M. H. Youn, W. Lee, K. T. Park, K. Gothandapani, A. N. Grace and S. K. Jeong, *ACS Omega*, 2020, **5**, 23919–23930.

52 M. Bin Mobarak, M. S. Hossain, F. Chowdhury and S. Ahmed, *Arabian J. Chem.*, 2022, **15**, 104117.

53 D. Mubarak Ali, J. Arunkumar, P. Pooja, G. Subramanian, N. Thajuddin and N. S. Alharbi, *Saudi Pharm. J.*, 2015, **23**, 421–428.

54 M. Zeraati, V. Alizadeh, P. Kazemzadeh, M. Safinejad, H. Kazemian and G. Sargazi, *J. Porous Mater.*, 2022, **29**, 257–267.

55 Z. Wei, H. Qiao, H. Yang, L. Zhu and X. Yan, *J. Nanomater.*, 2009, **2009**(1), 795928.

56 F. T. Alshorifi, S. M. El Dafrawy and A. I. Ahmed, *ACS Omega*, 2022, **7**, 23421–23444.

57 I. Gul, S. M. Khan, T. Mehmood, Z. Ahmad, H. Badshah and H. Shah, *Microsc. Res. Tech.*, 2020, **83**, 1124–1131.

58 B. Orhan, R. Adetoro and H. Kaygusuz, *ChemRxiv*, 2022, 1–11.

59 S. Li, K. Yang, P. Ye, K. Ma, Z. Zhang and Q. Huang, *Appl. Surf. Sci.*, 2020, **503**, 144090.

60 M. S. Rahmanifar, H. Hesari, A. Noori, M. Y. Masoomi, A. Morsali and M. F. Mousavi, *Electrochim. Acta*, 2018, **275**, 76–86.

61 S. Wang, W. Deng, L. Yang, Y. Tan, Q. Xie and S. Yao, *ACS Appl. Mater. Interfaces*, 2017, **9**, 24440–24445.

62 I. Z. Luna, L. N. Hilary, A. M. S. Chowdhury, M. A. Gafur, N. Khan and R. A. Khan, *OALib*, 2015, **02**, 1–8.

63 I. Markova-Deneva, *J. Univ. Chem. Technol. Metall.*, 2010, **45**, 351–378.

64 M. Abbasi, T. Noor, N. Iqbal and N. Zaman, *Int. J. Energy Res.*, 2022, **46**, 13915–13930.

65 S. Gopi, A. M. Al-Mohaimeed, W. A. Al-onazi, M. Soliman Elshikh and K. Yun, *J. King Saud Univ., Sci.*, 2021, **33**, 101379.

66 G. Guo, *J. Mater. Sci.: Mater. Electron.*, 2021, **32**, 16287–16301.

67 R. Liang, L. Shen, F. Jing, W. Wu, N. Qin, R. Lin and L. Wu, *Appl. Catal., B*, 2015, **162**, 245–251.

68 Z. Z. Ma, Y. S. Wang, B. Liu, H. Jiao and L. Xu, *Chemosensors*, 2022, **10**, 416.

69 Z. Li, D. Ren, Z. Wang, S. Jiang, S. Zhang, X. Zhang and W. Chen, *Water Sci. Technol.*, 2022, **86**, 80–94.

70 J. Yang, C. Zheng, P. Xiong, Y. Li and M. Wei, *J. Mater. Chem. A*, 2014, **2**, 19005–19010.

71 M. A. Moreira, M. P. S. Santos, C. G. Silva, J. M. Loureiro, J. S. Chang, C. Serre, A. F. P. Ferreira and A. E. Rodrigues, *Adsorption*, 2018, **24**, 715–724.

72 M. Amiri, Z. Tofighi, A. Khodayari, A. Bezaatpour, S. Sohrabnezhad, V. Mishyn, R. Boukherroub and S. Szunerits, *Appl. Organomet. Chem.*, 2020, **34**, 1–10.

73 F. Ming, J. Hou, D. Huo, J. Zhou, M. Yang, C. Shen, S. Zhang and C. Hou, *Anal. Methods*, 2019, **11**, 4382–4389.

74 M. T. Al-helaly and N. A. Al-Tememee, *J. Kufa phys.*, 2021, **13**(1), 33–42.

75 A. Eslami, N. M. Juibari, S. G. Hosseini and M. Abbasi, *Cent. Eur. J. Energ. Mater.*, 2017, **14**, 152–168.

76 H. Fan, F. Bahmani, Y. V. Kaneti, Y. Guo, A. A. Alothman, X. Wu, Y. Yamauchi, W. Li and J. Zhang, *Chem.–Eur. J.*, 2020, **26**, 13652–13658.

77 C. Zhang, H. Wang, Y. Nie, W. Yu and J. Yan, *Funct. Mater. Lett.*, 2020, **13**(6), 2050029.

78 D. Acharyya, K. Y. Huang, P. P. Chattopadhyay, M. S. Ho, H. J. Fecht and P. Bhattacharyya, *Analyst*, 2016, **141**, 2977–2989.

79 A. C. Vilbert, Y. Liu, H. Dai and Y. Lu, *Curr. Opin. Electrochem.*, 2021, **30**, 100780.

80 Y. Wu, Q. Hou, F. Li, Y. Sang, M. Hao, X. Tang, F. Qiu and H. Zhang, *Catalysts*, 2023, **13**(7), 1118.

81 K. Bergamaski, A. L. N. Pinheiro, E. Teixeira-Neto and F. C. Nart, *J. Phys. Chem. B*, 2006, **110**, 19271–19279.

82 A. Zaher, W. M. A. El Rouby and N. A. M. Barakat, *Fuel*, 2020, **280**, 118654.

83 S. Shahrokhian and S. Rezaee, *Electrochim. Acta*, 2018, **259**, 36–47.

84 K. J. Vetter and S. Barnatt, *J. Electrochem. Soc.*, 1968, **115**, 262.

85 W. Wang, Y. Li and H. Wang, *Micro Nano Lett.*, 2013, **8**, 23–26.

86 D. Escalera-López, Y. Niu, J. Yin, K. Cooke, N. V. Rees and R. E. Palmer, *ACS Catal.*, 2016, **6**, 6008–6017.

87 C. C. L. McCrory, S. Jung, I. M. Ferrer, S. M. Chatman, J. C. Peters and T. F. Jaramillo, *J. Am. Chem. Soc.*, 2015, **137**, 4347–4357.

88 J. Li, Y. Zuo, J. Liu, X. Wang, X. Yu, R. Du, T. Zhang, M. F. Infante-Carrió, P. Tang, J. Arbiol, J. Llorca, Z. Luo and A. Cabot, *J. Mater. Chem. A*, 2019, **7**, 22036–22043.

89 N. Wang, S. Liang, L. Zhang, P. Cao, L. Xu and M. Lin, *Colloids Surf., A*, 2020, **603**, 125199.

90 J. Ma, X. Wang, Z. Chu, J. Zhang, P. Du, Q. Zhang, F. Cao and J. Liu, *ChemCatChem*, 2021, **13**, 4824–4832.

91 Y. Wang, C. Liu, J. Xiang, L. Xing, X. Ou, S. Chen, X. Xue, F. Yu and R. Li, *Int. J. Electrochem. Sci.*, 2016, **14**, 5247–5258.

92 C. Eßbach, I. Senkovska, T. Unmüssig, A. Fischer and S. Kaskel, *ACS Appl. Mater. Interfaces*, 2019, **11**, 20915–20922.

93 W. Tu and Y. H. Chin, *J. Catal.*, 2014, **313**, 55–69.

94 A. Brunetti, M. Migliori, D. Cozza, E. Catizzone, G. Giordano and G. Barbieri, *ACS Sustainable Chem. Eng.*, 2020, **8**, 10471–10479.

95 T. Noor, M. Mohtashim, N. Iqbal, S. Raza, N. Zaman, L. Rasheed and M. Yousuf, *J. Electroanal. Chem.*, 2021, **890**, 115249.